 © The Authors. CC BY 4.0 Int. Licencee: SV-JME

# Fracture Analysis of Laminated Composite Plates Reinforced with Carbon Nanotubes (CNTs)

Mehmet N. Balci[1,✉] – Arda Çalışkan[1,2] – Bora Yıldırım[1]

1 Department of Mechanical Engineering, Hacettepe University, Beytepe Campus, 06800, Ankara, Türkiye
2 Turkish Aerospace Industries Inc., Kahramankazan, 06980, Ankara, Türkiye

✉ mehmetbalci@hacettepe.edu.tr

**Abstract** *This study investigates the influence of carbon nanotube reinforcement on the fracture behavior of laminated composite plates. Using classical laminated plate theory and the displacement correlation technique integrated with the finite element method, stress intensity factors are calculated for various carbon nanotube volume fractions, fiber orientations, crack lengths, and dispersion types. The research also examines how carbon nanotube-related factors such as waviness and agglomeration affect the stress intensity factor in different composite structures. A mesh convergence study is performed to determine a suitable mesh size. The results are compared with those reported in the literature, and very good agreement is obtained. This comparison verifies the method and demonstrates that the displacement correlation technique can be used to accurately calculate stress intensity factors and investigate the fracture behavior of composites reinforced with nanotubes. The influence of carbon nanotube inclusion on the fracture behavior of carbon fiber laminated composites using a computational framework has not previously been addressed, which constitutes the novelty of the present work. Parametric studies show that carbon nanotube reinforcement has a substantial effect on the stress intensity factor. This effect varies with the fiber orientation angle, which appears to have a greater influence on the stress intensity factor than the nanotube content. The main findings show that adding carbon nanotubes up to a certain content can reduce the stress intensity factor in composites, particularly when the load is applied along the fiber orientation. These results can help guide the selection of carbon nanotube inclusion to improve the fracture behavior of these structures.*

**Keywords** *carbon nanotube (CNT), classical laminated plate theory, displacement correlation technique (DCT), effective composite laminate, stress intensity factor (SIF)*

**Highlights**

- *Fracture behavior of CNT-reinforced laminated composite plates was examined.*
- *DCT was implemented in crack model for a CNT-reinforced composite.*
- *CNT inclusion can improve fracture resistance in composites with fibers oriented along the loading direction.*
- *Waviness and agglomeration substantially affect fracture behavior, highlighting the importance of homogeneous CNT dispersion.*

## 1 INTRODUCTION

Composite materials are widely used in various industries, including the automotive, marine, aerospace, and construction sectors. These materials are designed to create structures with particular properties, such as high strength, stiffness, toughness, and low weight [1]. A prime example is the Boeing 787 Dreamliner, which incorporates approximately 50 % composite materials by weight, a significant increase compared to the 12 % used in the Boeing 777 [2]. Among the various reinforcements used in composites, carbon nanotubes (CNTs) stand out due to their exceptional structural and thermal properties. Since their discovery by Iijima [3], CNTs have garnered significant interest owing to their extraordinary mechanical characteristics, including tensile strength ranging from 11 GPa to 63 GPa and elastic moduli between 270 GPa and 950 GPa [4-6]. Carbon nanotubes are among the strongest and stiffest materials discovered to date in terms of tensile strength and elastic modulus, respectively [7]. CNTs have attracted considerable attention and have been used in nanoelectronic devices [8,9], probe tips for scanning probe microscopes [10,11] and aerospace and automotive applications [12,13]. Due to their excellent mechanical and electrical properties, a new generation of composite materials with relatively low carbon nanotube loadings (<10 wt.%) in polymer matrices is expected to be needed for various future applications [14,15]. Their nanoscale dimensions and high aspect ratios enable effective load transfer and crack bridging, especially when the nanotubes are uniformly dispersed within the matrix [16]. To estimate the mechanical properties of CNT-reinforced composites, micromechanical modeling techniques are frequently employed. The rule of mixtures (RoM) provides a simple and commonly used approach to predict elastic modulus or strength based on the volume fractions and individual properties of the constituents. Mirzaei and Kiani [17] investigated nonlinear free vibration of functionally graded CNT-reinforced composite plates, using a refined RoM to determine the effective material properties. While RoM is useful for continuous and well-aligned fiber reinforcements, it does not consider critical factors such as fiber aspect ratio, load transfer efficiency, interfacial bonding, or reinforcement orientation. To address these limitations, the Halpin-Tsai model offers an improved formulation, initially developed for short-fiber composites, by introducing an empirical shape factor that relates the composite modulus to the matrix and reinforcement properties [18]. This model was further refined by Georgantzinos et al. [19], who developed mathematical models of CNT reinforcement and incorporated the unique effects of CNTs, such as waviness, orientation, dispersion, and agglomeration. Fracture mechanics plays a critical role in understanding and predicting failure mechanisms in composite laminates, where anisotropy and heterogeneity present unique analytical challenges. A key parameter in fracture analysis is the stress intensity factor (SIF), which governs crack initiation and crack growth under applied loads. SIFs were

 DOI: 10.5545/sv-jme.2026.1696

determined experimentally for a reinforced polyester composite under different fracture modes [20]. Hsieh et al. [21] experimentally investigated the effect of CNT inclusion on the fracture toughness and fatigue performance of a thermosetting epoxy polymer. Mourad et al. [22] demonstrated that CNT reinforcement could improve fracture toughness by increasing the resistance to crack propagation, particularly under Mode I (opening) and Mode II (sliding) loading conditions. Parhizgar et al. [23] examined the applicability of linear elastic fracture mechanics principles to orthotropic composite materials. Hosseini et al. [24] reviewed the performance of fiber-reinforced composite laminates with carbon nanotubes. Abot et al. [25] reported that nano-reinforced laminated composites containing a CNT array exhibited improved interlaminar properties, providing a new approach to mitigating delamination in laminated composites. Cho [26] conducted a computational study comparing static bending, free vibration and mechanical buckling between cracked graphene platelet-reinforced and CNT-reinforced composite plates in the linear and nonlinear regimes using the two-dimensional (2D) extended natural element method. Delamination behavior of layered orthotropic functionally graded coatings under thermal loading conditions was investigated by Yildirim et al. [27], who employed the displacement correlation technique (DCT) to calculate SIFs at the crack tip. DCT has been widely utilized in combination with the finite element method (FEM) as a computationally efficient scheme alternative to energy-based methods such as the J-integral and the virtual crack closure technique (VCCT) in linear elastic fracture mechanics. DCT uses the displacement fields around the crack tip to calculate the SIF, which makes it particularly suitable for parametric studies. Kim and Paulino [28] developed modified crack closure methods to analyze mixed-mode fracture of orthotropic functionally graded materials based on FEM. Kaman [29] studied the effect of fiber orientation on fracture toughness of laminated composite plates with a symmetric laminate configuration $[0/\theta]_s$ using classical laminated plate theory. Mohammed et al. [30] examined the natural frequencies of a laminated nanocomposite containing equal numbers of glass and carbon fiber layers, using classical laminated plate theory within an analytical framework. Kiran et al. [31] investigated the prediction of the fracture toughness of epoxy-carbon fabric-CNT composites using the Taguchi method and machine learning. It was reported that adding 0.5 wt.% CNT fillers improved fracture toughness by up to 15 %. Yu et al. [32] experimentally characterized the Mode I fracture toughness and stress-life (S-N) curve of multi-walled carbon nanotube (MWCNT)-reinforced epoxy matrix composites, and found that incorporating MWCNTs into the matrix significantly improved fracture toughness and fatigue life. Cho [33] determined the SIFs at cracks in functionally graded CNT-reinforced epoxy composites with different CNT volume fractions. Fatigue crack growth analysis for a CNT-reinforced polymer composite was performed by Dwivedi et al. [34], using a wide range of CNT volume fractions to demonstrate the effectiveness of the proposed method. In fact, the CNT content within the matrix ranges from approximately 0.5 wt.% to 5.0 wt.% in many studies since this range appears suitable for manufacturing CNT-containing composites in practice. Nevertheless, the present study considers a broader range of CNT contents based on the adopted micromechanical model.

Accurate determination of SIF plays a crucial role in both fracture and fatigue-life analysis of carbon fiber/epoxy composites with a hybrid matrix involving MWCNTs. A thorough review of the existing literature indicates that fracture behavior of laminated composites involving CNTs within the polymer matrix has received relatively limited attention, particularly with respect to the combined effects of CNT reinforcement, lay-up configuration, and crack geometry. The present study addresses this research gap by systematically investigating the influence of CNT reinforcement on the fracture behavior of a plate by integrating DCT into FEM. In particular, the effects of different ply lay-up orientations, CNT inclusion, and crack lengths on the SIF are examined. Two representative crack configurations, namely double-edge-crack (DEC) and center-crack (CC) models, are considered to provide a comprehensive assessment of the role of CNT reinforcement in different cases. The study therefore aims to establish a clear understanding of how CNT inclusion and laminate configuration interact to affect the fracture behavior of these structures.

## 2 METHODS AND MATERIALS

The problem considered is illustrated in Fig. 1 for two different configurations: the DEC model and the CC model. The loading is perpendicular to the crack plane; therefore, only Mode I is considered.

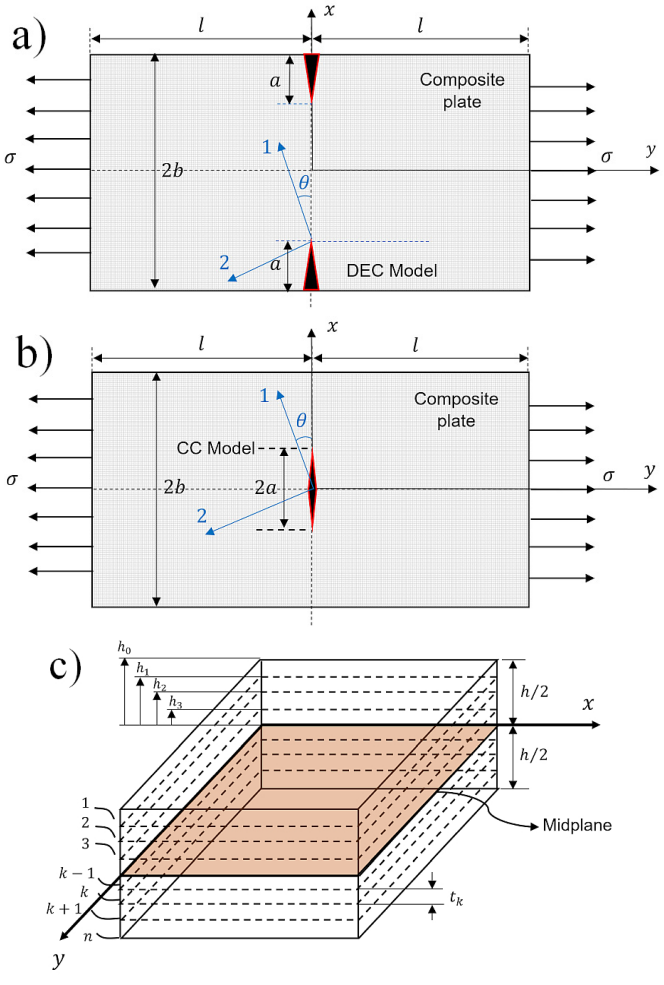



**Fig. 1. a) DEC, b) CC composite plates with fiber orientation angle $\theta$, and c) a schematic of an n-ply laminated composite plate**

The plate is made of a composite containing carbon fibers embedded in a hybrid polymer matrix reinforced with CNTs. $2a$ denotes the center crack length, $a$ denotes the edge crack length. $2b$, $2l$ and $h$ denote the plate width, height and thickness, respectively. $\theta$ is the fiber orientation angle.

### 2.1 Classical Laminated Plate Theory (CLPT)

CLPT serves as a fundamental approach for studying and understanding the behavior of composite laminate structures. Its core principles are based on the plate deformation assumptions in Kirchhoff's hypothesis, which focuses on the analysis of thin plates. According to Kirchhoff's hypothesis, the plate's thickness undergoes negligible change during deformation, and initially planar sections normal to the mid-surface remain planar and perpendicular to the mid-surface after deformation [35]. This assumption simplifies the analysis by considering transverse shear deformations to be minimal, which makes it possible to derive the in-plane stress-strain equations for CLPT. The displacements are written as:

$$u = u_0 - z\frac{\partial w_0}{\partial x}, \quad v = v_0 - z\frac{\partial w_0}{\partial y}, \tag{1}$$

where $w_0$ is the transverse deformation. The out-of-plane strain components are zero, which results in $\varepsilon_{zz} = \gamma_{xz} = \gamma_{yz} = 0$. The in-plane strain components are expressed as:

$$\varepsilon_{xx} = \frac{\partial u}{\partial x}, \quad \varepsilon_{yy} = \frac{\partial v}{\partial y}, \quad \varepsilon_{xy} = \frac{1}{2}\left(\frac{\partial u}{\partial y} + \frac{\partial v}{\partial x}\right). \tag{2}$$

Under plane stress conditions, substituting Eq. (1) into Eq. (2) yields the following relation:

$$\begin{bmatrix} \varepsilon_{xx} \\ \varepsilon_{yy} \\ \gamma_{xy} \end{bmatrix} = \begin{bmatrix} \varepsilon_{xx}^{\,0} \\ \varepsilon_{yy}^{\,0} \\ \gamma_{xy}^{\,0} \end{bmatrix} + z\begin{bmatrix} \kappa_{xx} \\ \kappa_{yy} \\ \kappa_{xy} \end{bmatrix}, \tag{3}$$

where $\varepsilon_{xx}^0, \varepsilon_{yy}^0$, and $\gamma_{xy}^0$ are the midplane normal strains and engineering shear strains, respectively, and $\gamma_{xy}^0 = 2\varepsilon_{xy}^0$. The midplane strain and the curvature are written as:

$$\begin{bmatrix} \varepsilon_{xx}^0 \\ \varepsilon_{yy}^0 \\ \gamma_{xy}^0 \end{bmatrix} = \begin{bmatrix} \dfrac{\partial u_0}{\partial x} \\ \dfrac{\partial v_0}{\partial y} \\ \dfrac{\partial u_0}{\partial y} + \dfrac{\partial v_0}{\partial x} \end{bmatrix}, \quad \begin{bmatrix} \kappa_{xx} \\ \kappa_{yy} \\ \kappa_{xy} \end{bmatrix} = -\begin{bmatrix} \dfrac{\partial^2 w_0}{\partial x^2} \\ \dfrac{\partial^2 w_0}{\partial y^2} \\ 2\dfrac{\partial^2 w_0}{\partial x \partial y} \end{bmatrix}. \tag{4}$$

The key assumption for a unidirectional lamina is that of plane stress, since the lamina thickness is small relative to its width and length. In the absence of out-of-plane loads, the following relations are valid:

$$\sigma_{33} = \tau_{13} = \tau_{23} = 0, \tag{5}$$

$$\gamma_{13} = \gamma_{23} = 0. \tag{6}$$

Based on the plane stress assumption, strain-stress relations can be written in terms of the compliance matrix [$S$] as:

$$\begin{bmatrix} \varepsilon_{11} \\ \varepsilon_{22} \\ \gamma_{12} \end{bmatrix} = \begin{bmatrix} S_{11} & S_{12} & 0 \\ S_{12} & S_{22} & 0 \\ 0 & 0 & S_{66} \end{bmatrix} \begin{bmatrix} \sigma_{11} \\ \sigma_{22} \\ \sigma_{12} \end{bmatrix}. \tag{7}$$

The elements of the compliance matrix [$S$] are written as follows:

$$S_{11} = \frac{1}{E_{11}}, S_{12} = \frac{-\nu_{12}}{E_{11}} = \frac{-\nu_{21}}{E_{22}}, S_{22} = \frac{1}{E_{22}}, S_{66} = \frac{1}{G_{12}}, \frac{\nu_{12}}{E_{11}} = \frac{\nu_{21}}{E_{22}}, \tag{8}$$

where $E_{11}$ and $E_{22}$, are the elastic moduli in the longitudinal and transverse directions, respectively. $\nu_{12}$ is the major Poisson's ratio and $\nu_{21}$ is the minor Poisson's ratio of the lamina. $G_{12}$ is the in-plane shear modulus. The reduced stiffness matrix [$Q$] is obtained by taking the inverse of the compliance matrix.

$$\begin{bmatrix} \sigma_{11} \\ \sigma_{22} \\ \tau_{12} \end{bmatrix} = \begin{bmatrix} Q_{11} & Q_{12} & 0 \\ Q_{12} & Q_{22} & 0 \\ 0 & 0 & Q_{66} \end{bmatrix} \begin{bmatrix} \varepsilon_{11} \\ \varepsilon_{22} \\ \gamma_{12} \end{bmatrix}. \tag{9}$$

The elements of the stiffness matrix are calculated from the compliance values as follows:

$$Q_{11} = \frac{S_{22}}{S_{11}S_{22} - S_{12}^2}, \quad Q_{12} = -\frac{S_{12}}{S_{11}S_{22} - S_{12}^2},$$
$$Q_{22} = \frac{S_{11}}{S_{11}S_{22} - S_{12}^2}, \quad Q_{66} = \frac{1}{S_{66}}. \tag{10}$$

For an angle-ply lamina, none of the terms in the compliance matrix are zero. Note that $x$ and $y$ denote the axes of the global coordinate system, whereas 1 and 2 denote those of the local coordinate system as depicted in Fig. 1. The angle $\theta$ indicates the rotation between the global and local systems. The stresses in the global coordinate system are transformed to the local system as follows:

$$\begin{bmatrix} \sigma_{xx} \\ \sigma_{yy} \\ \tau_{xy} \end{bmatrix} = [T]^{-1} \begin{bmatrix} \sigma_{11} \\ \sigma_{22} \\ \tau_{12} \end{bmatrix}. \tag{11}$$

Therefore, the stress-strain relation for an angle-ply lamina is:

$$\begin{bmatrix} \sigma_{xx} \\ \sigma_{yy} \\ \tau_{xy} \end{bmatrix} = \begin{bmatrix} \overline{Q_{11}} & \overline{Q_{12}} & \overline{Q_{16}} \\ \overline{Q_{12}} & \overline{Q_{22}} & \overline{Q_{26}} \\ \overline{Q_{16}} & \overline{Q_{26}} & \overline{Q_{66}} \end{bmatrix} \begin{bmatrix} \varepsilon_{xx} \\ \varepsilon_{yy} \\ \gamma_{xy} \end{bmatrix}, \tag{12}$$

To determine the stiffness matrix for plies at different angles, [$R$] and [$T$] matrices are needed. The matrices [$R$] and [$T$] are Reuter's matrix and the transformation matrix, respectively. The transformed reduced stiffness matrix $\left[\overline{Q}\right]_\theta$ is calculated as:

$$\left[\overline{Q}\right]_\theta = [T]^{-1}[Q]_0[R][T][R]^{-1}, \tag{13}$$

Reuter's matrix and the transformation matrix are provided in the Appendix. The elements of the reduced stiffness matrix are $\overline{Q_{ij}}$, $(i,j = 1,2,6)$. Composite structures are frequently subjected to normal stresses due to bending and axial loads and shear stresses due to twisting. The stress-strain relationship for the composite laminate, incorporating the midplane strains and curvatures, can be written as:

$$\begin{bmatrix} \sigma_{xx} \\ \sigma_{yy} \\ \tau_{xy} \end{bmatrix} = \begin{bmatrix} \overline{Q_{11}} & \overline{Q_{12}} & \overline{Q_{16}} \\ \overline{Q_{12}} & \overline{Q_{22}} & \overline{Q_{26}} \\ \overline{Q_{16}} & \overline{Q_{26}} & \overline{Q_{66}} \end{bmatrix}_k \left\{ \begin{bmatrix} \varepsilon_{xx} \\ \varepsilon_{yy} \\ \gamma_{xy} \end{bmatrix} + z\begin{bmatrix} K_{xx} \\ K_{yy} \\ K_{xy} \end{bmatrix} \right\}. \tag{14}$$

By integrating Eq. (14) with respect to the thickness coordinate $z$, the resultant moments and forces are calculated using the lamina thickness as follows [35]:

$$\begin{bmatrix} N_x \\ N_y \\ N_{xy} \end{bmatrix} = \sum_{k=1}^{n} \begin{bmatrix} \overline{Q_{11}} & \overline{Q_{12}} & \overline{Q_{16}} \\ \overline{Q_{12}} & \overline{Q_{22}} & \overline{Q_{26}} \\ \overline{Q_{16}} & \overline{Q_{26}} & \overline{Q_{66}} \end{bmatrix} \left\{ \int_{h_{k-1}}^{h_k} \begin{bmatrix} \varepsilon_{xx} \\ \varepsilon_{yy} \\ \gamma_{xy} \end{bmatrix} dz + \int_{h_{k-1}}^{h_k} \begin{bmatrix} K_{xx} \\ K_{yy} \\ K_{xy} \end{bmatrix} z dz \right\}, \tag{15}$$

$$\begin{bmatrix} M_x \\ M_y \\ M_{xy} \end{bmatrix} = \sum_{k=1}^{n} \begin{bmatrix} \overline{Q_{11}} & \overline{Q_{12}} & \overline{Q_{16}} \\ \overline{Q_{12}} & \overline{Q_{22}} & \overline{Q_{26}} \\ \overline{Q_{16}} & \overline{Q_{26}} & \overline{Q_{66}} \end{bmatrix} \left\{ \int_{h_{k-1}}^{h_k} \begin{bmatrix} \varepsilon_{xx} \\ \varepsilon_{yy} \\ \gamma_{xy} \end{bmatrix} z dz + \int_{h_{k-1}}^{h_k} \begin{bmatrix} K_{xx} \\ K_{yy} \\ K_{xy} \end{bmatrix} z^2 dz \right\}, \tag{16}$$

where $N_x$, $N_y$ and $N_{xy}$ are the in-plane normal and shear loads and $M_x$, $M_y$ and $M_{xy}$ are the resultant bending moments. Figure 1c depicts the composite laminated plate comprising $n$ plies with different orientations. $t_k$ denotes the thickness of each lamina and is given by $t_k = (h_k - h_{k-1})$. The detailed procedure for calculating the effective properties of the

composite laminate, such as the elastic modulus and Poisson's ratio, was provided by Kaman [29].

## 2.2 The Influence of CNT Reinforcement

The unidirectional carbon fibers are embedded in a hybrid matrix comprising epoxy resin and MWCNTs. A schematic view of the unidirectional carbon fiber lamina is shown in Fig. 2.

The parameters $A$ and $W$ define the amplitude and wavelength of the MWCNT, respectively. The dependence of the properties of CNT-reinforced polymer nanocomposites on the CNT volume fraction, CNT aspect ratio, and constituent material properties can be estimated by the Halpin-Tsai (H-T) micromechanical method [36-39]. It was observed in the results of Hassanzadeh-Aghdam and Jamali [39] that the H-T model modified to account for random orientation, waviness, and agglomeration predicts elastic moduli in good agreement with experimental results for CNT volume fractions up to 10 %. The Young's modulus of the CNT-reinforced polymer matrix is calculated using the H-T method as provided in [18,19,39]:

$$E_{m-CNT} = E_m\left(\frac{1+2R\delta V_{CNT}}{1-\delta V_{CNT}}\right). \tag{17}$$

A critical factor for CNT reinforcement in the matrix is the orientation factor $f_R$ which takes a value of 1/3 or 1/6 under two different conditions [40]. If the thickness of the composite is significantly less than the CNT length, $f_R$ is 1/3. If the CNT length is much smaller than the thickness of the composite, $f_R$ is 1/6. The parameter $\delta$ is calculated as follows [18,19,39]:

$$\delta = \frac{\left(f_R f_W f_A E_{CNT}/E_m\right)-1}{\left(f_R f_W f_A E_{CNT}/E_m\right)+2R}, \tag{18}$$

where $R$ is the aspect ratio of the CNT, given by:

$$R = L_{CNT}/d_{CNT}, \tag{19}$$

where $L_{CNT}$ and $d_{CNT}$ denote the length and diameter of the CNT, respectively. The waviness of the CNT is quantified as follows:

$$f_W = 1-\left(A/W\right), \tag{20}$$

The dispersion of CNTs in the polymer matrix also affects the elastic properties of the matrix. This effect is accounted for using the agglomeration factor as follows:

$$f_A = e^{\left(-\alpha V_{CNT}{}^{\beta}\right)}, \tag{21}$$

where the parameters $\alpha$ and $\beta$ are used to express the degree of agglomeration. The elastic modulus in the longitudinal direction and the Poisson's ratio of a single lamina are calculated as follows:

$$E_1 = E_f V_f + E_{m-CNT} V_{m-CNT}, \tag{22}$$

$$v_{12} = v_f V_f + v_{m-CNT} V_{m-CNT}, \tag{23}$$

where $E_f$, $V_f$ and $v_f$ are the elastic modulus, volume percentage and Poisson's ratio of the fiber, respectively. The transverse elastic modulus, modulus of rigidity, and transverse Poisson's ratio are calculated using the H-T method as follows [18,19]:

$$P = P_m\left(\frac{1+\xi\eta V_f}{1-\eta V_f}\right), \quad \eta = \frac{\left(P_f/P_m\right)-1}{\left(P_f/P_m\right)+\xi}, \tag{24}$$

where $P_m$ denotes CNT-reinforced matrix properties, $P_f$ denotes fiber properties, and $P$ represents a general material property corresponding to any of the following four properties, namely the transverse elastic modulus $E_2$, transverse Poisson's ratio $v_{23}$, and the modulus of rigidity $G_{12}$, and $G_{23}$. Generally, $\xi$ is taken as 2 for determining $E_2$, and 1 for determining $v_{23}$, $G_{12}$ and $G_{23}$.

## 2.3 Implementation of the Displacement Correlation Technique in the Finite Element Method

The individual plies are not modeled explicitly as a layered composite in the finite element model. The multilayer laminate is represented as an equivalent single-layer composite and the contribution of the individual plies is incorporated through CLPT using effective laminate properties. The resulting effective laminate constants are used to represent a homogeneous equivalent orthotropic continuum. The carbon fibers, epoxy matrix and CNTs are not modeled explicitly as separate phases in the finite element model. The laminate is represented in the finite element model as a single equivalent orthotropic layer rather than as individual plies. Due to the symmetry in both geometry and loading, a quarter model is employed in the finite element analyses. The thickness of the equivalent layer is $h$ = 1.235 mm. The quarter plate model has in-plane dimensions of $l$ = 50 mm and $b$ = 10 mm. A uniform tensile stress of 1 MPa (unity) is applied perpendicular to the crack plane to produce pure Mode I loading. Several techniques are used to calculate SIFs in isotropic and orthotropic structures. These include VCCT, the J-integral, DCT, and standardized physical testing [27,29]. Among them, DCT is computationally efficient and straightforward to implement in FEM. Even though energy methods give more accurate results, DCT is still a valid and widely used method in the literature for SIF calculations [27]. The only requirement is to record the displacements of prescribed nodes along the $x$- and $y$-axes in the finite element model and use these nodal displacement values to calculate $K_I$ and $K_{II}$. For general orthotropic materials, Mode I and Mode II SIFs are calculated as provided in [27]:

$$K_I = \frac{\sqrt{2\pi}}{4\sqrt{S_{22}D_0}}\frac{\Delta v}{\sqrt{r}}, \quad K_{II} = \frac{\sqrt{2\pi}}{4\sqrt{S_{22}D_0}}\frac{\Delta u}{\sqrt{r}}, \tag{25}$$

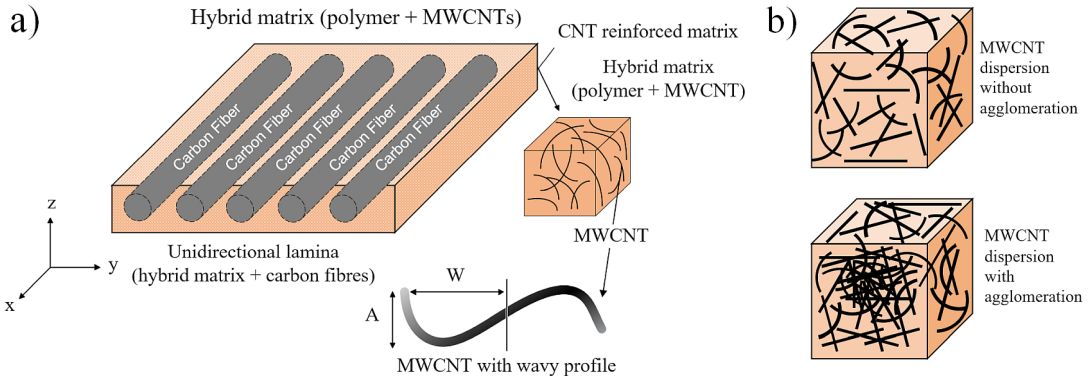



**Fig. 2. a) MWCNT inclusion in the polymer/epoxy matrix of a carbon fiber-reinforced lamina, and b) MWCNT dispersion in the polymer/epoxy matrix showing agglomeration**

$$\Delta u = u(r,\pi) - u(r,-\pi), \quad \Delta v = v(r,\pi) - v(r,-\pi), \tag{26}$$

$$D_0 = \sqrt{2\sqrt{S_{11}S_{22}} + 2S_{12} + S_{66}}, \tag{27}$$

Substituting Eq. (26) into Eq. (25) yields the following relations:

$$K_{\mathrm{I}} = \frac{\sqrt{2\pi}}{4\sqrt{S_{22}}D_0}\lim_{r\to 0}\left(\frac{v(r,\pi)-v(r,-\pi)}{\sqrt{r}}\right),$$
$$K_{\mathrm{II}} = \frac{\sqrt{2\pi}}{4\sqrt{S_{22}}D_0}\lim_{r\to 0}\left(\frac{u(r,\pi)-u(r,-\pi)}{\sqrt{r}}\right), \tag{28}$$

The term in the limit is approximated by a linear polynomial as $r\to 0$, and Eq. (29) is obtained after the necessary mathematical manipulations. As illustrated in Fig. 3, nodes 2 and 4 are located on the inner circle with a radius of $R_2$ whereas nodes 3 and 5 are located on the outer circle with a radius of $R_3$. The vertical displacements at nodes 2, 4, 3 and 5 are expressed as: $v_{12}=v(R_2,\pi)$, $v_{14}=v(R_2,-\pi)$, $v_{13}=v(R_3,\pi)$, and $v_{15}=v(R_3,-\pi)$. Analogous expressions can be obtained for the horizontal displacements $u_{12}$, $u_{14}$, $u_{13}$, and $u_{15}$.

$$\frac{v(R_2,\pi)-v(R_2,-\pi)}{\sqrt{R_2}} = \frac{v_{12}-v_{14}}{\sqrt{R_2}} = AR_2 + B,$$
$$\frac{v(R_3,\pi)-v(R_3,-\pi)}{\sqrt{R_3}} = \frac{v_{13}-v_{15}}{\sqrt{R_3}} = AR_3 + B. \tag{29}$$

Since the plate thickness is relatively small with respect to its width and height, the plane stress assumption is used in DCT. The stress intensity factor at the crack tip within a very large plate under uniform tensile loading is $K_\infty$, which can be calculated as $K_\infty = \sigma\sqrt{\pi a}$. The SIF strongly depends on geometry, crack size and absolute stress level. The normalized SIF quantifies the influence of a particular configuration on the stress field in the vicinity of the crack tip. Normalization decouples the geometric and loading variables, allowing the individual effects of parameters such as CNT content, fiber orientation angle, crack length ratio, and agglomeration on the SIF to be examined. Thus, geometric and loading parameters are isolated through the normalization procedure. The factors of absolute stress level and absolute crack length were removed, and normalized Mode I SIF becomes a dimensionless form. The normalized Mode I SIF can be written as:

$$K_{\mathrm{In}} = K_{\mathrm{I}}/K_\infty, \tag{30}$$

Since the laminated plate is loaded under uniform tension and the crack is located perpendicular to the loading, the quarter model can be considered in FEM in order to reduce the computational power. It is obvious that laminated composite plates are subjected to uniform tensile load at left edge boundary, which makes problem purely an Opening mode (Mode I) without any in-plane shear or Mode II loads. Thus, $K_{\mathrm{II}} \cong 0$. The boundary conditions for the DEC and CC problems are illustrated in Figs. 4a and b, respectively. Figure 4c depicts 8-noded quadrilateral elements, quarter point singular finite elements at a crack. Coordinate systems $(x,y)$ and $(\xi,\eta)$ denote the physical and isoparametric coordinate systems, respectively, available in ANSYS [41]. Quarter-point singular elements are formulated by relocating the mid-side nodes of standard quadrilateral elements to the quarter-point position. Instead of placing the node in the middle of two corner nodes, this mid-side node is positioned at one quarter of the edge length away from the crack tip. Thus, these elements yield more accurate SIFs. The crack tip is taken as the reference point for the displacement calculation. $R_2$ and $R_3$ denote the radial distances measured from the crack tip to the selected nodes within the refined crack-tip region, with $R_3=4R_2$ according to the adopted DCT formulation. Nodal displacements are recorded using suitable commands. A key feature of PLANE183 is its compatibility with quarter-point singular elements, which are placed around the crack tip. In FEM simulations, PLANE183 quadrilateral planar elements are utilized with the plane stress option.

The crack-tip element size is 0.02 mm, with 18 circumferential divisions and a radial growth ratio of 1.5. Away from the crack-tip region, the mesh is gradually coarsened to a nominal element size of 0.20 mm. The model contains 15168 elements for a crack length of $a$ = 3 mm. Effective composite laminate theory is employed to convert the multilayer laminate into an equivalent orthotropic material characterized by the effective engineering constants $E_x$, $E_y$, $G_{xy}$ and $\nu_{xy}$. These effective orthotropic properties are directly assigned to the PLANE183 elements.

## 3 RESULTS AND DISCUSSION

In this section, SIFs are obtained for the carbon fiber laminated composite plate reinforced with CNTs. The properties of the epoxy resin, carbon fibers, and CNTs are given in Table 1. Experimental results show that the elastic modulus and tensile strength of polymer nanocomposites can be considerably enhanced by adding a small percentage of CNTs [42]. The volume fractions of carbon fibers and the epoxy matrix are taken as 60 % and 40 %, respectively [19]. The materials used are AS4 carbon fibers, 3501-6 epoxy resin, and MWCNTs.

**Table 1. Fiber, resin and CNT properties [19,42,43]**

| Carbon AS4 | | Epoxy resin 3501-6 | | MWCNT | |
|---|---|---|---|---|---|
| $E_{f11}$ [GPa] | 225 | $E_m$ [GPa] | 4.2 | $E_{CNT}$ [GPa] | 900 |
| $E_{f22}$ [GPa] | 15 | $G_m$ [GPa] | 1.567 | $L_{CNT}$ [nm] | 2000 |
| $G_{f12}$ [GPa] | 15 | $\nu_m$ [-] | 0.34 | $d_{CNT}$ [nm] | 30 |
| $G_{f23}$ [GPa] | 7 | $\rho_m$ [kg/m$^3$] | 1250 | $\rho_{CNT}$ [kg/m$^3$] | 2250 |
| $\nu_{f12}$[-] | 0.20 | | | | |
| $\nu_{f23}$[-] | 0.40 | | | | |
| $\rho_f$[kg/m$^3$] | 1800 | | | | |

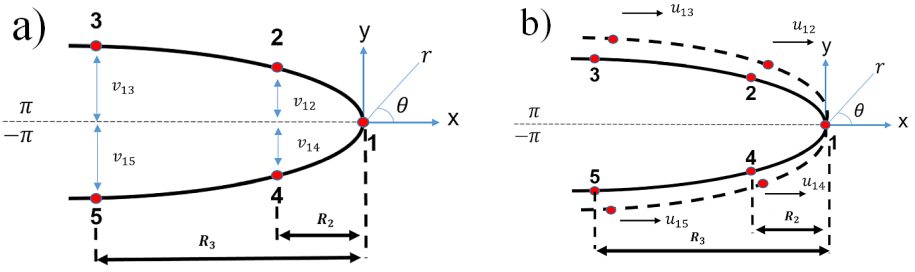



**Fig. 3. Normal displacements around the crack-tip region; a) nodal displacements in the y-direction, and b) nodal displacements in the x-direction**

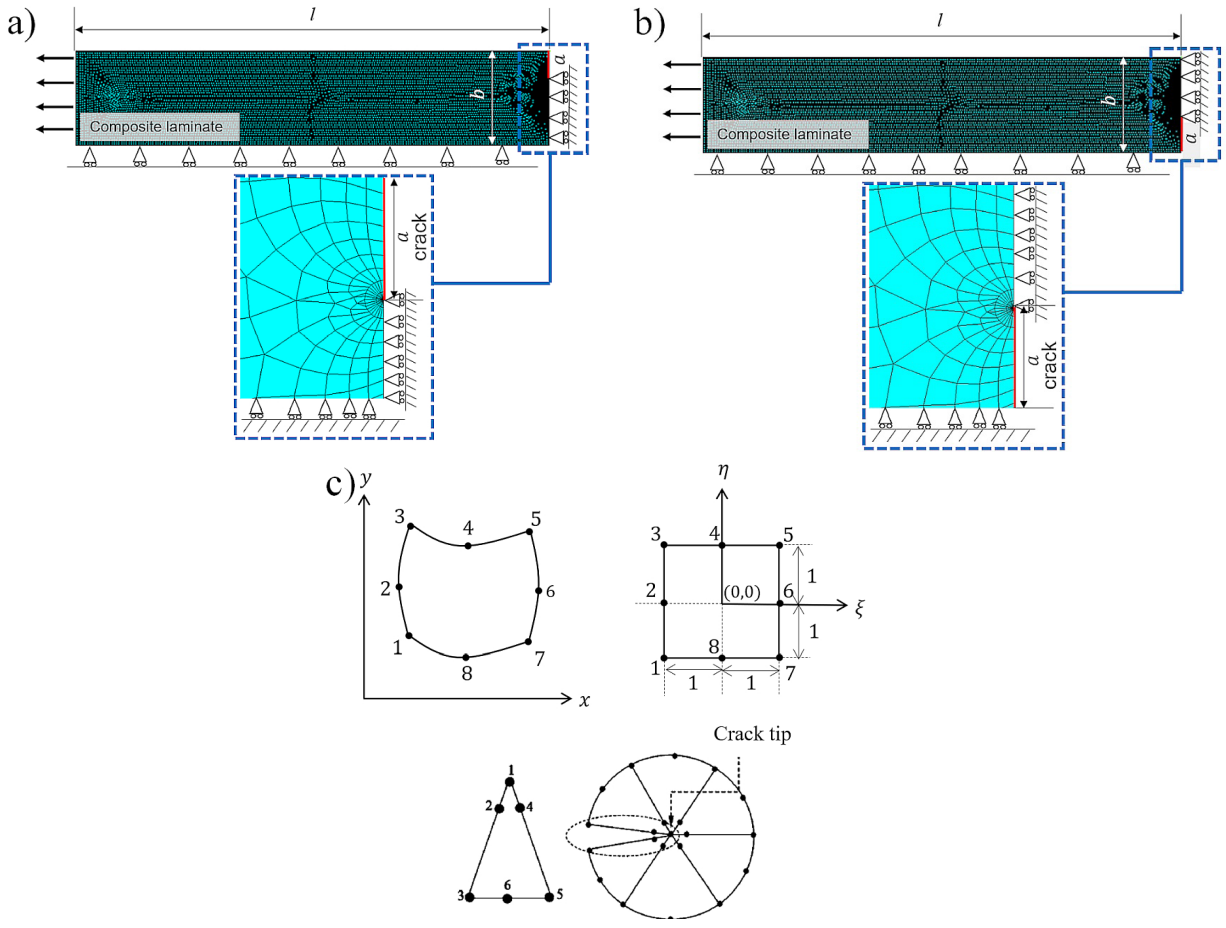



Fig. 4. Finite element meshes with applied loads and boundary conditions for a) the DEC model, b) the CC model, and c) eight-node rectangular quadrilateral elements and singular quarter-point finite elements used in the analysis

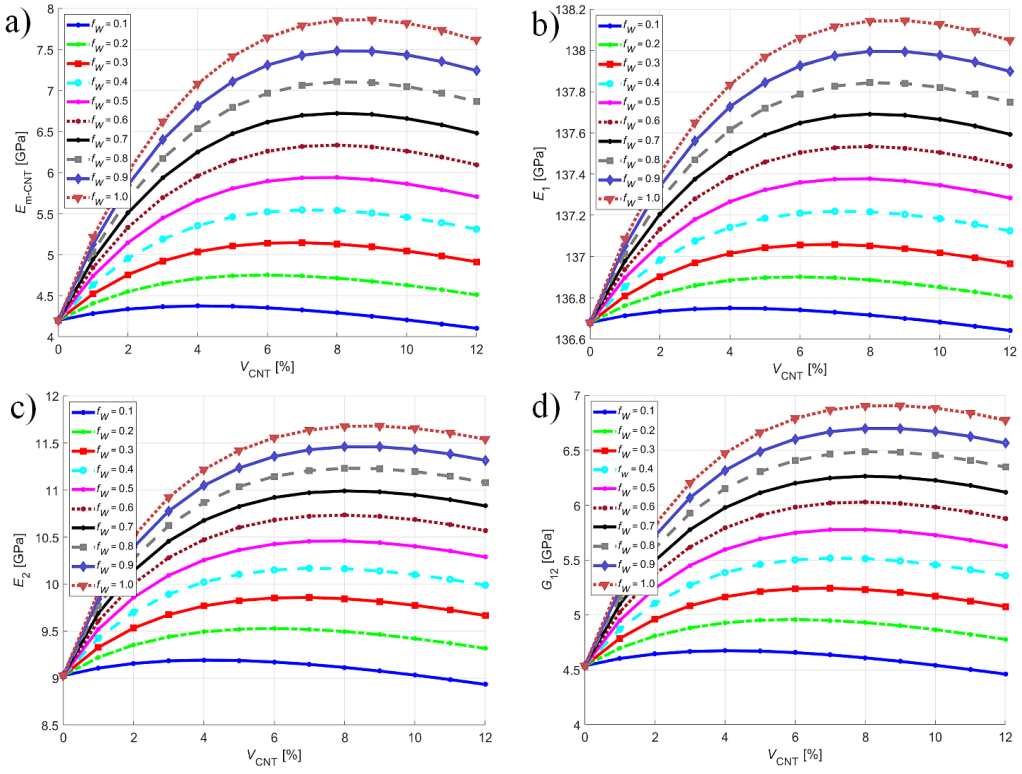



Fig. 5. Effects of waviness and CNT volume fraction on material properties; a) epoxy matrix elastic modulus $E_{m\text{-}CNT}$, b) elastic modulus in the longitudinal direction $E_1$ c) elastic modulus in the transverse direction $E_2$, and d) in-plane shear modulus $G_{12}$

The CNT content can be expressed as either a volume percentage [%] or a weight percentage [wt.%]. The relationship between them is given by Cho [33]:

$$V_{CNT} = \frac{w_{CNT}}{w_{CNT} + (\rho_{CNT}/\rho_m) - (\rho_{CNT}/\rho_m) w_{CNT}}. \quad (31)$$

where $V_{CNT}$, $w_{CNT}$, $\rho_{CNT}$, $\rho_m$ denote the volume percentage, weight percentage, CNT density, and matrix density, respectively. Although 5.0 wt.% CNT inclusion corresponds to a volume fraction of 2.84 %, the present study examines a broad range of CNT inclusion to clarify its effects on fracture behavior. However, the CNT contents used in experimental studies [20,21] are considerably lower than the volume fractions considered in this study due to physical limitations during the manufacture of matrix materials with CNT inclusion. The turning point around 8 % CNT should be regarded as a prediction of the adopted effective property model, which is dependent upon the present micromechanical modeling framework and the CNT dispersion parameters [19]. Therefore, 8 % CNT inclusion is the model-predicted turning point, which may not be practically realized experimentally. At high CNT concentrations, practical limitations associated with CNT dispersion, agglomeration, viscosity and manufacturing should also be considered. The present study proposes a computational method to elucidate the fracture behavior of laminated composites with various CNT volume fractions using a parametric approach. Figure 5 graphically shows the influence of CNT reinforcement and the waviness factor on the matrix elastic properties. As shown in the graphs, as $V_{CNT}$ is increased, the epoxy matrix stiffens up to a CNT volume fraction of 8 %.

Beyond this level, the stiffness of the matrix tends to decrease. If the waviness factor $f_W$ is small and close to 0, it indicates highly wavy CNTs and if $f_W$ is close to 1, this implies straight CNTs. Therefore, an increase in $f_W$ corresponds to straighter CNTs and a stiffer matrix. It was reported by Song and Youn [44] that the tensile modulus of the nanocomposite increases with increasing CNT loading regardless of the dispersion. The agglomerates of the CNTs reduce the apparent volume fraction of the polymer matrix. At low CNT concentrations, the well-dispersed nanotubes effectively transfer load from the polymer matrix and enhance the stiffness and strength of the composite. However, beyond an optimum CNT concentration, strong van der Waals forces induce CNT agglomeration and network formation, while the increasing viscosity of the CNT/polymer mixture hinders homogeneous dispersion and polymer wetting. CNT-rich regions, weak interfacial zones and processing-induced voids act as stress concentrators and crack initiation sites. Consequently, the effective load transfer efficiency decreases and further inclusion of CNTs can lead to reductions in the stiffness and strength of the nanocomposite. Figure 6 displays the matrix properties as functions of CNT volume fraction and the agglomeration parameter. When the agglomeration parameter $\alpha$ is zero, it indicates perfectly homogeneous CNT dispersion and when $\alpha$ is increased, it indicates greater agglomeration, and a further increase in $\alpha$ induces very inhomogeneous dispersion. As shown, increased agglomeration leads to a decline in the elastic properties of the matrix beyond a certain CNT volume fraction.

Tables 2 and 3 present the longitudinal elastic modulus $E_x$, transverse elastic modulus $E_y$, shear modulus $G_{xy}$ and the major Poisson's ratio $v_{xy}$ with respect to various CNT contents for $[0°/15°/15°/15°]_s$ and $[0°/90°/0°/90°]_s$ plates, respectively. $\Delta$ indicates the percentage difference between reinforced and unreinforced elastic properties. As $V_{CNT}$ is increased, the longitudinal $E_x$ and transverse $E_y$ elastic moduli increase more substantially for $[0°/15°/15°/15°]_s$ than for $[0°/90°/0°/90°]_s$. Moreover, an increase in CNT volume fraction results in a remarkable increase in the shear modulus $G_{xy}$ for $[0°/15°/15°/15°]_s$ and $[0°/90°/0°/90°]_s$ configurations.

Before the parametric analysis, mesh convergence and comparison studies are performed. The mesh convergence study assesses how

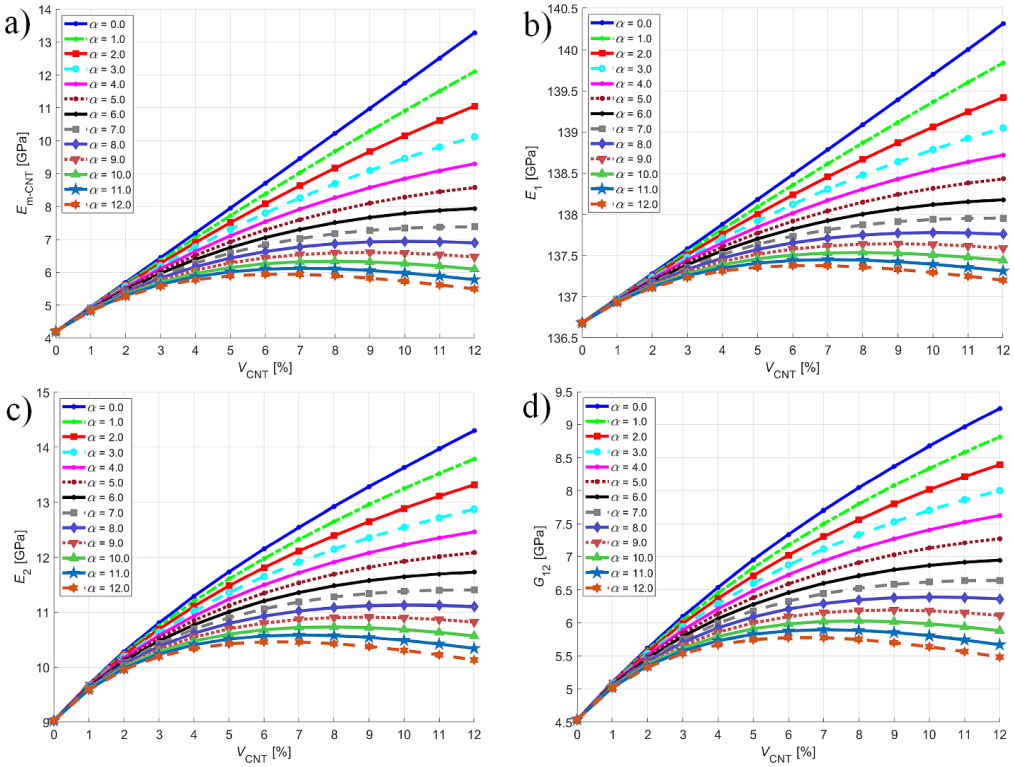



**Fig. 6. Effects of agglomeration and CNT volume fraction on material properties; a) epoxy matrix elastic modulus $E_{m\text{-}CNT}$, b) elastic modulus in the longitudinal direction $E_1$, c) elastic modulus in the transverse direction $E_2$, and d) in-plane shear modulus $G_{12}$**

**Table 2. Mechanical properties of a laminate $[0°/15°/0°/15°]_s$ with different volume fractions of CNT**

| $V_{CNT}$ [%] | $E_x$ [GPa] | $\Delta E_x$ [%] | $E_y$ [GPa] | $\Delta E_y$ [%] | $G_{xy}$ [GPa] | $\Delta G_{xy}$ [%] | $v_{xy}$ [-] | $\Delta v_{xy}$ [%] |
|---|---|---|---|---|---|---|---|---|
| 0 | 76.3597 | 0.00 | 9.1399 | 0.00 | 6.4055 | 0.00 | 0.4143 | 0.00 |
| 2 | 81.0576 | 6.15 | 10.1775 | 11.35 | 7.2187 | 12.69 | 0.3895 | -5.99 |
| 4 | 83.2297 | 9.00 | 10.6786 | 16.83 | 7.6256 | 19.05 | 0.3786 | -8.64 |
| 6 | 84.1735 | 10.23 | 10.9017 | 19.28 | 7.8089 | 21.91 | 0.3739 | -9.76 |
| 8 | 84.4047 | 10.54 | 10.9569 | 19.88 | 7.8545 | 22.62 | 0.3728 | -10.03 |
| 10 | 84.1848 | 10.25 | 10.9045 | 19.31 | 7.8112 | 21.94 | 0.3739 | -9.77 |
| 12 | 83.6643 | 9.57 | 10.7809 | 17.95 | 7.7095 | 20.36 | 0.3764 | -9.16 |

**Table 3. Mechanical properties of a laminate $[0°/90°/0°/90°]_s$ with different volume fractions of CNT**

| $V_{CNT}$ [%] | $E_x$ [GPa] | $\Delta E_x$ [%] | $E_y$ [GPa] | $\Delta E_y$ [%] | $G_{xy}$ [GPa] | $\Delta G_{xy}$ [%] | $v_{xy}$ [-] | $\Delta v_{xy}$ [%] |
|---|---|---|---|---|---|---|---|---|
| 0 | 73.0958 | 0.00 | 73.0958 | 0.00 | 4.5365 | 0.00 | 0.0317 | 0.00 |
| 2 | 73.8318 | 1.01 | 73.8318 | 1.01 | 5.3718 | 18.41 | 0.0348 | 9.76 |
| 4 | 74.2025 | 1.51 | 74.2025 | 1.51 | 5.7924 | 27.68 | 0.0363 | 14.35 |
| 6 | 74.3710 | 1.74 | 74.3710 | 1.74 | 5.9823 | 31.87 | 0.0369 | 16.37 |
| 8 | 74.4131 | 1.80 | 74.4131 | 1.80 | 6.0295 | 32.91 | 0.0371 | 16.87 |
| 10 | 74.3731 | 1.75 | 74.3731 | 1.75 | 5.9846 | 31.92 | 0.0369 | 16.40 |
| 12 | 74.2795 | 1.62 | 74.2795 | 1.62 | 5.8793 | 29.60 | 0.0366 | 15.28 |

**Table 4. Mode I SIF calculated in mesh convergence study for the DEC model**

| Case # | Mesh size [mm] | Mode I SIF $\left[\text{MPa}\sqrt{\text{mm}}\right]$ | $\Delta$ [%] |
|---|---|---|---|
| 1 | 0.15 | 1.45599 | 0.82 |
| 2 | 0.1 | 1.45423 | 0.70 |
| 3 | 0.05 | 1.44926 | 0.35 |
| 4 | 0.02 | 1.44424 | 0.0035 |
| 5* | 0.005 | 1.44419 | - |

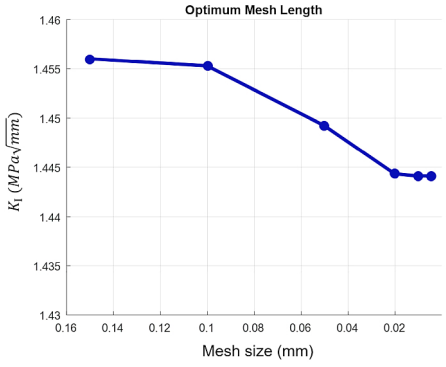



**Table 5. Comparison of Mode I SIF between Irwin [45], Tada et al. [46], and the present study for the DEC model**

| Crack length ratio, ($a/b$) | Irwin [45] $\left[\text{MPa}\sqrt{\text{mm}}\right]$ | Tada et al. [46] $\left[\text{MPa}\sqrt{\text{mm}}\right]$ | Present $\left[\text{MPa}\sqrt{\text{mm}}\right]$ |
|---|---|---|---|
| 0.1 | 2.0033 | 1.9885 | 1.9820 |
| 0.2 | 2.8279 | 2.8167 | 2.7909 |
| 0.3 | 3.4546 | 3.4728 | 3.4267 |
| 0.4 | 4.0171 | 4.0734 | 4.0181 |
| 0.5 | 4.6113 | 4.6113 | 4.6391 |
| 0.6 | 5.3305 | 5.4143 | 5.3729 |
| 0.7 | 6.2725 | 6.3767 | 6.3521 |
| 0.8 | 7.5423 | 7.9067 | 7.8995 |

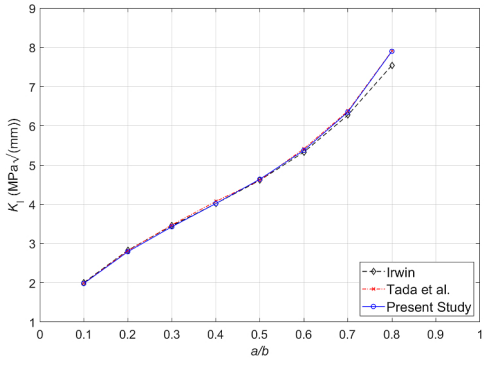
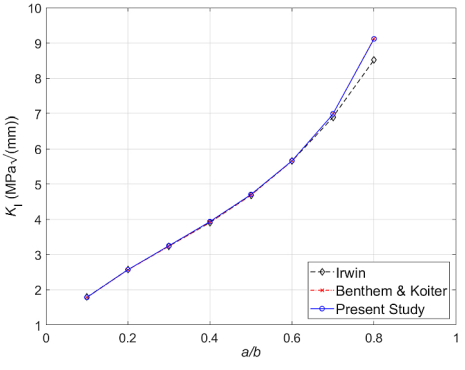



**Table 6. Comparison of Mode I SIFs from Irwin [45], Benthem and Koiter [47], and the present study for the CC model**

| Crack length ratio, ($a/b$) | Irwin [45] $\left[\text{MPa}\sqrt{\text{mm}}\right]$ | Benthem and Koiter [47] $\left[\text{MPa}\sqrt{\text{mm}}\right]$ | Present $\left[\text{MPa}\sqrt{\text{mm}}\right]$ |
|---|---|---|---|
| 0.1 | 1.7927 | 1.7817 | 1.780 |
| 0.2 | 2.5725 | 2.5627 | 2.570 |
| 0.3 | 3.2347 | 3.2368 | 3.250 |
| 0.4 | 3.9090 | 3.9192 | 3.940 |
| 0.5 | 4.6871 | 4.6914 | 4.710 |
| 0.6 | 5.6550 | 5.6544 | 5.670 |
| 0.7 | 6.9008 | 6.9882 | 6.990 |
| 0.8 | 8.5169 | 9.1280 | 9.120 |



mesh size affects the results. An 8-ply laminate with the configuration $[0°/15°/0°/15°]_s$ is considered in five different cases (Case 1, 2, …, 5). In the mesh convergence study, a rectangular laminated plate with $l$ = 50 mm and $b$ = 10 mm is selected as a test model, without CNT inclusion. The analysis is performed for the DEC model. The aim is to determine how reducing the mesh size at the crack tip affects the opening-mode SIF and to select a suitable mesh size. The SIF value generated in Case 5 is taken as the most accurate because it uses the finest mesh. Therefore, a superscript (*) is added to mark the reference. Δ represents the percentage difference between the SIF results for each case and those for the reference case. The percentage difference gradually decreases as the mesh size decreases. Hence, the finite element model in Case 4, with a mesh size of 0.02 mm around the crack tip, is used since Δ is below 0.005 %. Tables 5 and 6 compare the Mode I SIFs obtained in the present study with those available in the literature. The plate used is homogeneous and isotropic, without lamination through its thickness. The developed computer codes are adapted to analyze fracture in an isotropic homogeneous plate. This situation can be considered a special case for which benchmark results are available in literature. While Table 5 indicates Mode I SIF values for the DEC model, Table 6 presents values of Mode I SIF for the CC model. As can be seen in Table 5, the results of the present study and those provided by Irwin [45] and Tada et al. [46] agree very well in the DEC case. Moreover, if Mode I SIF values in Table 6 are examined further, it can be seen that the results of the present study are very close to those of Irwin [45] and Benthem and Koiter [47] in CC case. Hence, the results agree well with the benchmark solutions over the full range of crack length ratios except $a/b$=0.8 for the Irwin [45] model.

The difference between the finite element results and the analytical benchmark solution increases at the largest crack length, where $a/b$=0.8 since the remaining ligament becomes relatively small and finite-width effects are more pronounced. Jansen et al. [48] reported that, as long as $a/b$ is sufficiently small, this can be considered a good approximation to a finite-width center-cracked specimen: the accuracy is better than 5 % for $a/b \leq 0.25$. Hence, care is needed when calculating SIFs for larger cracks.

### 3.1 Effects of Key Parameters on SIF in DEC Model

In this section, the effects of key parameters on normalized Mode I SIF are analyzed. CNT volume fraction, fiber orientation, crack length, waviness and agglomeration are considered as key parameters which influence fracture behavior. The baseline values used in the analyses are $f_R$=1/6, $f_W$=0.6, $\alpha$=10, and $\beta$=0.9 unless otherwise stated. An orientation factor of $f_R$=1/6 is adopted since the CNT length is considerably smaller than the thickness of the composite layer. Figures 7a to d display displacement contours in the plate with the $[0°/0°/0°/0°]_s$ configuration, and Figs. 7e to h illustrate displacement contours in the plate with the $[90°/90°/90°/90°]_s$ configuration. The displacement contours change markedly with the ply orientation configuration; however, CNT inclusion has only a slight effect on the displacement fields around the crack.

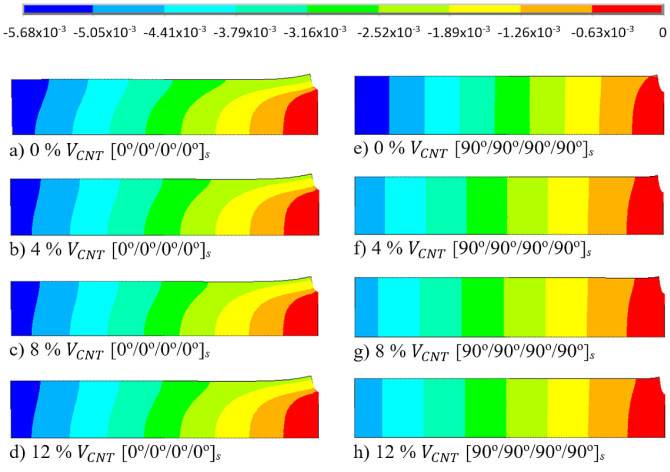



**Fig. 7. Displacement contours [m] in y direction within the laminated composite plate with different volume fractions of CNT**

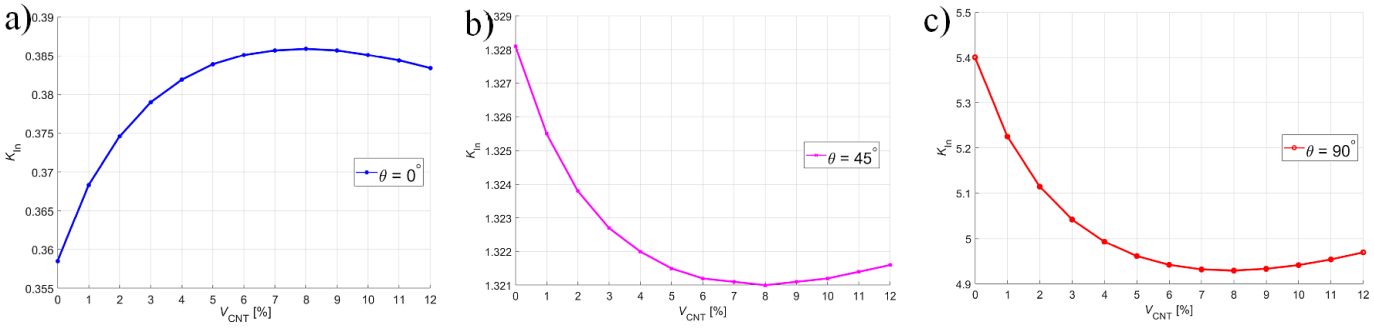



**Fig. 8. Influence of CNT volume fraction on the normalized Mode I SIF for the DEC model; a) $[0°/0°/0°/0°]_s$, b) $[45°/45°/45°/45°]_s$, and c) $[90°/90°/90°/90°]_s$**

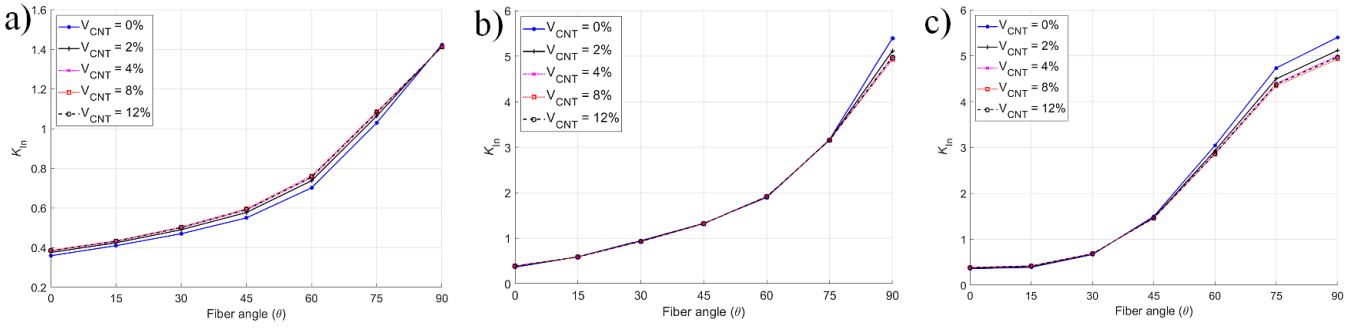



**Fig. 9. Influence of fiber orientation angle on the normalized Mode I SIF for the DEC model; a) $[0°/\theta/0°/\theta]_s$, b) $[\theta/\theta/\theta/\theta]_s$, and c) $[\theta/-\theta/\theta/-\theta]_s$**

Figures 8 and 9 show the effects of CNT volume fraction and fiber orientation angle on the Mode I SIF in the composite plate

An increase in $V_{CNT}$ leads to stiffening of both plates, as can be inferred from Fig. 7. The pattern of displacement contours is different for the $[0°/0°/0°/0°]_s$ and $[90°/90°/90°/90°]_s$ configurations. Moreover, it is obvious that stiffening of the $[90°/90°/90°/90°]_s$ configuration is greater since the displacement is smaller than that in the $[0°/0°/0°/0°]_s$ case. As shown in Fig. 8, the maximum SIF is obtained for the $[90°/90°/90°/90°]_s$ case whereas the minimum SIF is obtained for the $[0°/0°/0°/0°]_s$ configuration. Although an increase in the CNT volume fraction up to 8 % leads to an increase in the normalized Mode I SIF in the $[0°/0°/0°/0°]_s$ case, it results in a decrease in the SIF for the $[45°/45°/45°/45°]_s$ and $[90°/90°/90°/90°]_s$ cases. Thus, opposite trends are observed for different ply configurations. This behavior may be related to changes in the load-carrying mechanism associated with changes in $E_1$, $E_2$, $G_{12}$, and $v_{12}$, for different ply orientations. An increase in the CNT content helps the polymer matrix carry higher loads and improves load transfer between reinforcing fibers and the matrix. When $\theta$ = 90°, this mechanism becomes more prominent and may help reduce the Mode I SIF. CNT reinforcement at volume fractions up to 8 % in the $[45°/45°/45°/45°]_s$ and $[90°/90°/90°/90°]_s$ cases can reduce the normalized SIF value. The impact of the increase in the volume fraction of CNT on the normalized SIF for different ply configurations is examined and depicted in Fig. 9. An increase in $V_{CNT}$ produces slightly higher SIFs for the $[0°/\theta/0°/\theta]_s$; however, it leads to a small decrease in SIF for the $[\theta/\theta/\theta/\theta]_s$ and $[\theta/-\theta/\theta/-\theta]_s$ configurations. The largest increase in the Mode I SIF is seen around 45° in the $[0°/\theta/0°/\theta]_s$ case, whereas the greatest decrease in Mode I SIF occurs around 90° in the $[\theta/\theta/\theta/\theta]_s$ and $[\theta/-\theta/\theta/-\theta]_s$ cases. Figure 10 illustrates the impact of crack length on the normalized Mode I SIF. The normalized Mode I SIF is highest in the $[90°/90°/90°/90°]_s$ case when compared to other configurations. As the crack length ratio ($a/b$) is increased, the normalized SIF value increases for all considered laminate configurations: $[0°/15°/0°/15°]_s$, $[30°/-30°/30°/-30°]_s$ and $[90°/90°/90°/90°]_s$. While CNT inclusion leads to an increase in the Mode I SIF in the $[0°/15°/0°/15°]_s$ and $[30°/-30°/30°/-30°]_s$ cases, it results in lower values of Mode I SIF in the

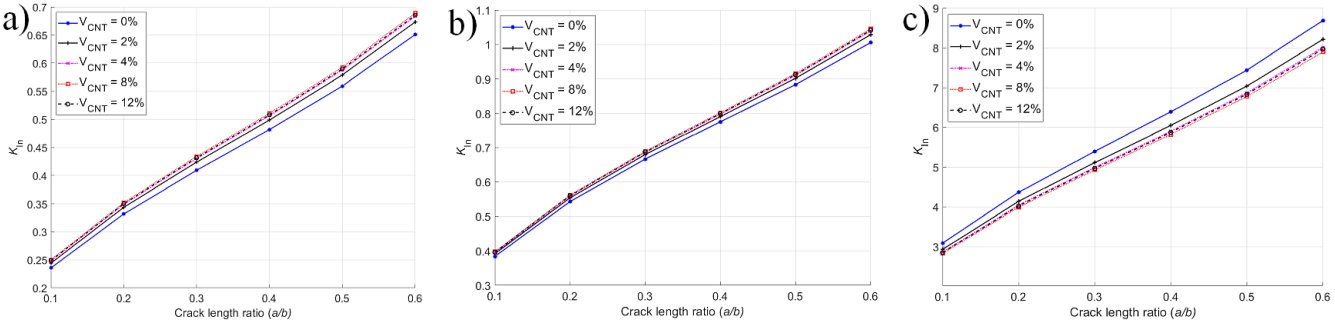



**Fig. 10. Influence of crack length ratio on the normalized Mode I SIF for the DEC model; a) $[0°/15°/0°/15°]_s$, b) $[30°/-30°/30°/-30°]_s$, and c) $[90°/90°/90°/90°]_s$**

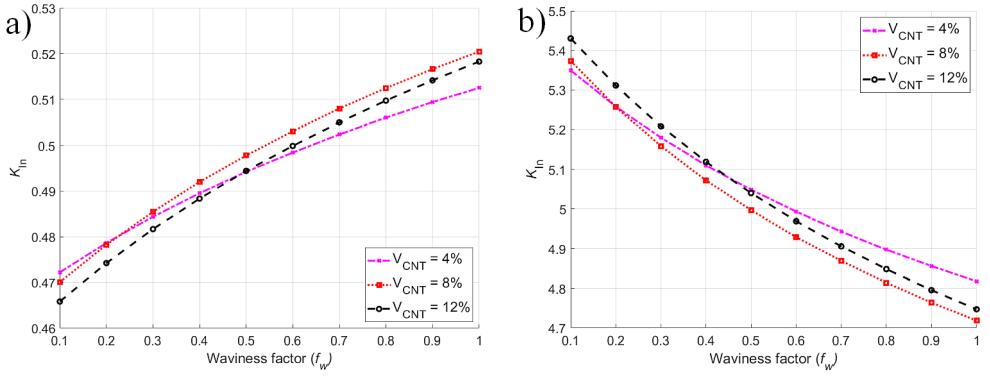



**Fig. 11. Influence of waviness factor on the normalized Mode I SIF; a) $[0°/30°/0°/30°]_s$, and b) $[90°/90°/90°/90°]_s$, for the DEC model**

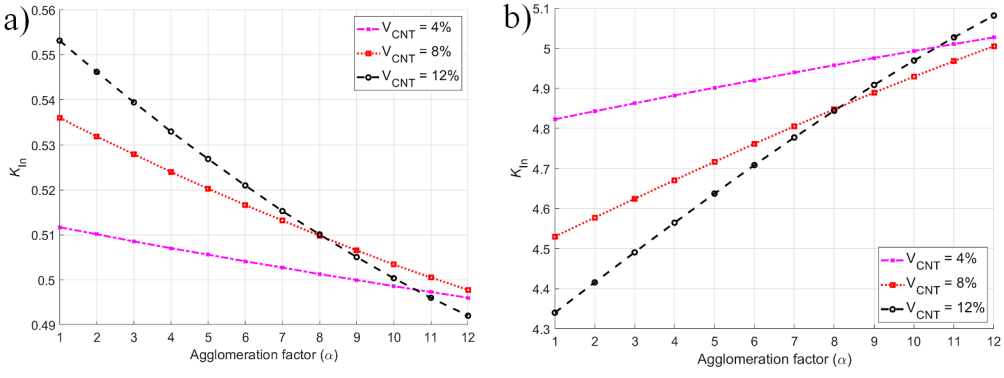



**Fig. 12. Influence of the agglomeration factor on the normalized Mode I SIF in the DEC model; a) $[0°/30°/0°/30°]_s$, and b) $[90°/90°/90°/90°]_s$**

$[90°/90°/90°/90°]_s$ case, and the difference between SIFs obtained for different $V_{CNT}$ values and $V_{CNT}$=0 % becomes substantial in this configuration. Therefore, CNT use in the $[90°/90°/90°/90°]_s$ configuration is a viable option for reducing the SIF at all crack lengths. Thus, incorporating CNTs into the polymer/epoxy matrix can reduce the SIF when the loading is aligned with the carbon fibers. Figure 11 displays the influence of waviness factor $f_W$ of the CNT on normalized Mode I SIF for $[0°/30°/0°/30°]_s$ and $[90°/90°/90°/90°]_s$ configurations, respectively. As the waviness factor is increased, i.e., straighter CNT dispersion, the Mode I SIF is increased in $[0°/30°/0°/30°]_s$ case, and it is decreased in $[90°/90°/90°/90°]_s$ case. Therefore, waviness factor has different effects depending on the ply orientation. It is clear that utilization of straight CNT dispersion is useful to reduce Mode I SIF for $[90°/90°/90°/90°]_s$ case.

Figure 12 illustrates the effect of the agglomeration factor $\alpha$ on the $[0°/30°/0°/30°]_s$ and $[90°/90°/90°/90°]_s$ configurations, respectively. As $\alpha$ is increased, corresponding to increased agglomeration, the normalized SIF decreases in the $[0°/30°/0°/30°]_s$ case and it is increased in the $[90°/90°/90°/90°]_s$ case. Hence, agglomeration has different effects on Mode I SIF for different ply orientations.

Increased agglomeration in the $[90°/90°/90°/90°]_s$ case leads to greater Mode I SIF value, which can make composite more vulnerable to fracture. It is inferred from these figures that the change in the Mode I SIF tends to be greater as the volume fraction of CNT is higher in both configurations.

### 3.2 Effects of Key Parameters on SIF in CC Model

In this section, the effect of the key parameters is analyzed for the CC plate. Normalized Mode I SIF values are calculated and direct comparison between SIF results obtained for DEC and CC models is performed. Table 7 shows results for DEC and CC models with percent difference values.

The normalized Mode I SIF decreases by approximately 2.3 % to 2.7 % in the $[0°/0°/0°/0°]_s$ and $[90°/90°/90°/90°]_s$ configurations. However, the decrease is approximately 6.4 % to 6.8 % in the $[45°/45°/45°/45°]_s$ configuration. Thus, the maximum decrease in the Mode I SIF occurs in the CC model with the $[45°/45°/45°/45°]_s$ configuration at all levels of CNT inclusion. Table 8 tabulates the normalized Mode I SIF values generated in the CC model for different fiber orientation angles with a $[\theta/-\theta/\theta/-\theta]_s$ configuration. Increasing the CNT volume fraction does not cause a significant change, since the percentage differences for all $V_{CNT}$ cases are almost identical.

However, the fiber orientation angle θ has a greater influence on the results. An increase in $\theta$ from 0° to 45° causes a considerable increase in the percentage difference and a further increase in θ from 45° to 90° leads to a decrease in the percentage differences. Thus, the fiber orientation angle has a greater influence than the CNT content, and the difference between the SIFs obtained for the DEC and CC models is greatest for $\theta$ = 45°. Table 9 indicates the normalized SIF values obtained for the DEC and CC models and the corresponding

**Table 7. Comparison of normalized SIF results of DEC and CC model with various CNT volume fractions for $[\theta/\theta/\theta/\theta]_s$, θ = 0°, 45°, 90°**

| $V_{CNT}$ [%] | $[0°/0°/0°/0°]_s$ | | | $[45°/45°/45°/45°]_s$ | | | $[90°/90°/90°/90°]s$ | | |
|---|---|---|---|---|---|---|---|---|---|
| | DEC $K_{In}$ | CC $K_{In}$ | Δ [%] | DEC $K_{In}$ | CC $K_{In}$ | Δ [%] | DEC $K_{In}$ | CC $K_{In}$ | Δ [%] |
| 0 | 0.3585 | 0.3503 | -2.29 | 1.3281 | 1.2384 | -6.75 | 5.4003 | 5.2770 | -2.28 |
| 2 | 0.3746 | 0.3652 | -2.51 | 1.3238 | 1.2376 | -6.51 | 5.1149 | 4.9868 | -2.5 |
| 4 | 0.3819 | 0.3719 | -2.62 | 1.3220 | 1.2373 | -6.41 | 4.9931 | 4.8630 | -2.61 |
| 6 | 0.3851 | 0.3748 | -2.67 | 1.3212 | 1.2372 | -6.36 | 4.9417 | 4.8106 | -2.65 |
| 8 | 0.3859 | 0.3756 | -2.67 | 1.3210 | 1.2371 | -6.35 | 4.9292 | 4.7981 | -2.66 |
| 10 | 0.3851 | 0.3748 | -2.67 | 1.3212 | 1.2372 | -6.36 | 4.9411 | 4.8101 | -2.65 |
| 12 | 0.3834 | 0.3732 | -2.66 | 1.3216 | 1.2372 | -6.39 | 4.9693 | 4.8386 | -2.63 |

**Table 8. Comparison of normalized SIF results for the DEC and CC models showing the effect of fiber orientation for $[\theta/-\theta/\theta/-\theta]_s$, θ = 0°, 15°, 30°, 45°, 60°, 75°, 90°**

| $\theta$ | $V_{CNT}$ = 4 % | | | $V_{CNT}$ = 8 % | | | $V_{CNT}$ = 12 % | | |
|---|---|---|---|---|---|---|---|---|---|
| | DEC $K_{In}$ | CC $K_{In}$ | Δ [%] | DEC $K_{In}$ | CC $K_{In}$ | Δ [%] | DEC $K_{In}$ | CC $K_{In}$ | Δ [%] |
| 0° | 0.3819 | 0.3719 | -2.63 | 0.3859 | 0.3756 | -2.68 | 0.3834 | 0.3732 | -2.65 |
| 15° | 0.4168 | 0.3958 | -5.03 | 0.4216 | 0.4004 | -5.04 | 0.4186 | 0.3975 | -5.05 |
| 30° | 0.6854 | 0.6197 | -9.58 | 0.6888 | 0.6236 | -9.47 | 0.6866 | 0.6211 | -9.54 |
| 45° | 1.4629 | 1.2876 | -11.99 | 1.4575 | 1.2852 | -11.82 | 1.4608 | 1.2866 | -11.93 |
| 60° | 2.8813 | 2.6045 | -9.61 | 2.8546 | 2.5843 | -9.47 | 2.8713 | 2.5971 | -9.55 |
| 75° | 4.3963 | 4.1742 | -5.05 | 4.3429 | 4.1236 | -5.05 | 4.3761 | 4.1552 | -5.05 |
| 90° | 4.9931 | 4.863 | -2.61 | 4.9292 | 4.7981 | -2.66 | 4.9693 | 4.8386 | -2.63 |

**Table 9. Comparison of normalized SIF results for the DEC and CC models at various crack lengths for $[30°/-30°/30°/-30°]_s$**

| $(a/b)$ | $V_{CNT}$ = 4 % | | | $V_{CNT}$ = 8 % | | | $V_{CNT}$ = 12 % | | |
|---|---|---|---|---|---|---|---|---|---|
| | DEC $K_{In}$ | CC $K_{In}$ | Δ [%] | DEC $K_{In}$ | CC $K_{In}$ | Δ [%] | DEC $K_{In}$ | CC $K_{In}$ | Δ [%] |
| 0.1 | 0.3954 | 0.3327 | -15.85 | 0.3974 | 0.3351 | -15.68 | 0.3961 | 0.3337 | -15.76 |
| 0.2 | 0.5589 | 0.4836 | -13.47 | 0.5618 | 0.4870 | -13.31 | 0.5599 | 0.4849 | -13.40 |
| 0.3 | 0.6854 | 0.6197 | -9.58 | 0.6888 | 0.6236 | -9.47 | 0.6866 | 0.6211 | -9.54 |
| 0.4 | 0.7979 | 0.7630 | -4.37 | 0.8020 | 0.7675 | -4.30 | 0.7995 | 0.7647 | -4.35 |
| 0.5 | 0.9104 | 0.9294 | 2.08 | 0.9153 | 0.9344 | 2.09 | 0.9121 | 0.9313 | 2.10 |
| 0.6 | 1.0389 | 1.1386 | 9.60 | 1.0449 | 1.1442 | 9.50 | 1.0412 | 1.1407 | 9.56 |

percentage differences for a $[30°/-30°/30°/-30°]_s$ configuration. As the crack length ratio ($a/b$) is increased from 0.1 to 0.4, the normalized Mode I SIF increases for both DEC and CC models. This increase in the SIF suggests a higher susceptibility of the plate to fracture. The comparison shows that the largest percentage difference is approximately 16 % at a ratio of 0.1. As the crack length ratio is increased from 0.1 to 0.5, the SIFs in the DEC and CC models become closer and the percentage difference decreases to approximately 2.1 %. A further increase in this ratio causes the percentage difference to increase again. An increase in $V_{CNT}$ does not change the Mode I SIF considerably. Thus, this parameter has less influence than the crack length ratio.

## 4 CONCLUSIONS

This study provides an insight into the effect of CNT reinforcement on the fracture behavior of laminated composite plates. Material properties are calculated using the micromechanical model previously developed in [19,39], and effective laminate properties are determined using CLPT. Two crack configurations are considered: the DEC and CC models. Normalized Mode I SIFs are computed using FEM integrated with DCT. Although the proposed framework provides a computationally efficient approach to examining fracture parameters, its accuracy may depend on the assumptions underlying the micromechanical modeling, CNT reinforcement formulation, and interfacial behavior, as well as the limitations of the LEFM approach. The key findings are as follows:

- According to the adopted micromechanical model, the optimal CNT volume fraction for improving the mechanical properties of a laminate is approximately 8 %; beyond this value, diminishing returns are observed. This value depends on the adopted model and should not be interpreted as a universal optimum, since determining the optimal CNT content requires extensive experimental validation.
- The normalized SIF values follow the order: SIF $[90°/90°/90°/90°]_s$ > SIF $[45°/45°/45°/45°]_s$ > SIF $[0°/0°/0°/0°]_s$. As the CNT volume fraction increases up to 8 %, the normalized Mode I SIF increases in the $[0°/0°/0°/0°]_s$ configuration. However, it decreases in the $[45°/45°/45°/45°]_s$ and $[90°/90°/90°/90°]_s$ configurations. Therefore, CNT reinforcement can reduce the SIF in the latter two configurations.
- As the fiber orientation angle $\theta$ increases from 0° to 90°, the normalized Mode I SIF increases for all ply lay-up configurations. The fiber orientation angle has a greater influence on the normalized Mode I SIF than the CNT content. Increasing the CNT volume fraction has different effects depending on the lay-up configuration: $[0°/\theta/0°/\theta]$s, $[\theta/\theta/\theta/\theta]_s$, or $[\theta/-\theta/\theta/-\theta]_s$. As the CNT content $V_{CNT}$ increases, the Mode I SIF increases for $[0°/\theta/0°/\theta]_s$ (with the largest increase around 45°) and decreases for $[\theta/\theta/\theta/\theta]_s$ and $[\theta/-\theta/\theta/-\theta]_s$ (with the largest decrease around $\theta$ = 90°). The reduction in the Mode I SIF in the latter two configurations may help reduce susceptibility to fracture.
- As expected, increasing the crack length results in higher normalized SIFs for all ply orientations. Although increasing the CNT volume fraction raises the SIFs in the $[0°/15°/0°/15°]_s$ and $[30°/-30°/30°/-30°]_s$ configurations, it reduces the SIFs in the $[90°/90°/90°/90°]_s$ configuration, confirming the previously observed trend.
- Increasing the waviness factor, which corresponds to straighter CNTs, increases the normalized Mode I SIF in the $[0°/30°/0°/30°]_s$ configuration. However, the same increase reduces the Mode I SIF in the $[90°/90°/90°/90°]_s$ configuration. Thus, reducing CNT waviness can reduce the Mode I SIF in the $[90°/90°/90°/90°]_s$ configuration.
- Increasing the agglomeration factor corresponds to greater agglomeration and a more inhomogeneous CNT dispersion within the hybrid matrix. As the agglomeration factor increases, the SIF decreases in the $[0°/30°/0°/30°]_s$ configuration. However, the opposite trend is observed in the $[90°/90°/90°/90°]_s$ configuration, where higher SIFs are obtained for composites with highly agglomerated CNTs. Homogeneous dispersion is therefore critical in this configuration.
- Normalized Mode I SIFs are also computed for the CC model, and the percentage differences relative to the DEC model are calculated. Although increasing the CNT volume fraction produces similar percentage differences within each configuration, the largest difference is observed for $[45°/45°/45°/45°]_s$. Thus, the SIF is most sensitive to crack type in this configuration. Furthermore, the percentage difference between the DEC and CC results is greatest at smaller crack length ratios, highlighting the importance of crack type for short cracks.

### Nomenclature

| | |
|---|---|
| $u,v$ | displacement components in horizontal and vertical directions, [m] |
| $w_0$ | out-of-plane midplane displacement, [m] |
| $\varepsilon^0_{ij}$ | midplane tensorial strain $i,j = x, y$, [-] |
| $\varepsilon_{ij}$ | tensorial strain, $i,j = x, y, z$ or $i,j$ = 1, 2, 3, [-] |
| $\gamma^0_{ij}$ | midplane engineering shear strain $i,j = x, y$, [-] |
| $\gamma_{ij}$ | engineering shear strain, $i,j = x, y, z$ or $i,j$ = 1, 2, 3, [-] |
| $\sigma_{ij}$ | stress components, $i,j = x, y$ or $i,j$ = 1, 2, 3, [MPa] |
| $\kappa_{ij}$ | curvature, $i,j = x, y$, [$m^{-1}$]. |
| $E_{ij}$ | Young's modulus, $i,j = x, y$ or $i,j$ = 1, 2, 3, [MPa] |
| $E_m$ | Young's modulus of the matrix, [MPa] |
| $S_{ij}$ | elements of the compliance matrix, i,j=1,2 or 6, [MPa]-1 |
| $Q_{ij}$ | elements of the stiffness matrix, $i,j$ = 1, 2 or 6, [MPa] |
| $N_{ij}$ | resultant loads applied to the plate, $i,j$ = 1, 2, [N] |
| $M_{ij}$ | resultant bending moment applied to the plate, $i,j$ = 1, 2, [Nm] |
| $f_R$ | CNT orientation factor, [-] |
| $f_W$ | CNT waviness factor, [-] |
| $f_A$ | CNT agglomeration factor, [-] |
| $R$ | aspect ratio of the CNT, [-] |
| $V_f$ | volume fraction, $i = f$ for fiber, $i = m$ - $CNT$ for reinforced matrix, [-] |
| $K_I$, $K_{II}$ | mode I and Mode II stress intensity factors, $\left[\text{MPa}\sqrt{\text{mm}}\right]$ |
| $K_{Im}$ | normalized Mode I stress intensity factor, [-] |
| $K\infty$ | mode I stress intensity factor for an infinitely wide plate, $\left[\text{MPa}\sqrt{\text{mm}}\right]$ |

### Appendix

$$[R]=\begin{bmatrix}1 & 0 & 0\\ 0 & 1 & 0\\ 0 & 0 & 2\end{bmatrix}, \tag{A1}$$

$$[T]=\begin{bmatrix}c^2 & s^2 & 2sc\\ s^2 & c^2 & -2sc\\ -sc & sc & c^2-s^2\end{bmatrix}, \tag{A2}$$

$$c:\cos(\theta),\quad s:\sin(\theta). \tag{A3}$$

## References


[1] Chawla, K.K. *Composite Materials: Science and Engineering*. Springer (2021) New York.

[2] Kesarwani, S. Polymer composites in aviation sector. *Int J Eng Res Technol 6* 518-525 (2017) **DOI:10.17577/ijertv6is060291**.

[3] Iijima, S. Helical microtubules of graphitic carbon. *Nature 354* 56-58 (1991) **DOI:10.1038/354056a0**.

[4] Yu, M.-F., Lourie, O., Dyer, M.J., Moloni, K., Kelly, T.F., Ruoff, R.S. Strength and breaking mechanism of multi-walled carbon nanotubes under tensile load. *Science 287* 637-640 (2000) **DOI:10.1126/science.287.5453.637**.

[5] Popov, V.N. Carbon nanotubes: properties and application. *Mater Sci Eng 43* 61-102 (2004) **DOI:10.1016/j.mser.2003.10.001**.

[6] Ajayan, P.M., Vajtai, R. Properties and applications of carbon nanotubes, In: Biro, L.P, Bernardo, C.A. Tibbetts, G.G. Lambin, P. (eds.) Carbon Filaments and Nanotubes: Common Origins, Differing Applications. NATO Science Series Springer Dordrecht, 372 315-330 (2001) **DOI:10.1007/978-94-010-0777-1_23**.

[7] Manikandan, N., Suresh Kumar, V.P., Siva Murugan, S., Rathis, G., Vishnu Saran, K., Shabariganesh, T.K. Carbon nanotubes and their properties-The review. *Mater Today Proc 47* 4682-4685 (2021) **DOI:10.1016/j.matpr.2021.05.543**.

[8] Bachtold, A., Hadley, P., Nakanishi, T., Dekker, C. Logic circuits with carbon nanotube transistors. *Science 294* 1317-1320 (2001) **DOI:10.1126/science.1065824**.

[9] Derycke, V., Martel, R., Appenzeller, J., Avouris, Ph. Carbon nanotube inter- and intramolecular logic gates. *Nano Lett 1* 453-456 (2001) **DOI:10.1021/nl015606f**.

[10] Nishijima, H., Kamo, S., Akita, S., Nakayama, Y. Hohmura, K.I. Yoshimura, S.H., Takeyasu, K. Carbon-nanotube tips for scanning probe microscopy: Preparation by a controlled process and observation of deoxyribonucleic acid. *Appl Phys Lett 74* 4061-4063 (1999) **DOI:10.1063/1.123261**.

[11] Hafner, J.H., Cheung, C.-L., Wooley, A.T., Lieber, C.M. Structural and functional imaging with carbon nanotube AFM probes. *Prog Biophys Mol Biol 77* 73-110 (2001) **DOI:10.1016/S0079-6107(01)00011-6**.

[12] Breuer, O., Sundararaj, U. Big returns from small fibers: A review of polymer/carbon nanotube composites. *Polym Compos 25* 630-645 (2004) **DOI:10.1002/pc.20058**.

[13] Wise, K.E., Park, C., Siochi, E.J., Harrison, J.S. Stable dispersion of single wall carbon nanotubes in polyimide: the role of noncovalent interactions. *Chem Phys Lett 391* 207-211 (2004) **DOI:10.1016/j.cplett.2004.04.096**.

[14] Ajayan, P.M., Schadler, L.S., Giannaris, C., Rubio, A. Single-walled carbon nanotube-polymer composites: Strength and weakness. Adv Mater 12 750-753 (2000) **DOI:10.1002/(SICI)1521-4095(200005)12:10<750::AID-ADMA750>3.0.CO;2-6**.

[15] Shaffer, M., Kinloch, I.A. Prospects for nanotube and nanofiber composites. *Compos Sci Technol 64* 2281-2282 (2004) **DOI:10.1016/j.compscitech.2004.01.018**.

[16] Coleman, J.N., Khan, U., Blau, W.J. Gun'ko, Y.K. Small but strong: A review of the mechanical properties of carbon nanotube-polymer composites. *Carbon 44* 1624-1652 (2006) **DOI:10.1016/j.carbon.2006.02.038**.

[17] Mirzai, M., Kiani, Y. Nonlinear free vibration of FG-CNT reinforced composite plates. *Struct Eng Mech 64* 381-390 (2017) **DOI:10.12989/sem.2017.64.3.381**.

[18] Affdl, J.C., Kardos, J.L. The Halpin-Tsai equations: A Review. *Polym Eng Sci 16* 344-352 (1976) **DOI:10.1002/pen.760160512**.

[19] Georgantzinos, S.K., Antoniou, P.A., Giannopoulos, G.I., Fatsis, A., Markolefas, S.I. Design of laminated composite plates with carbon nanotube inclusions against buckling: Waviness and agglomeration effects. *Nanomaterials 11* 2261-2283 (2021) **DOI:10.3390/nano11092261**.

[20] Olodu, D.D., Aliyegbenoma, C. Investigation of the stress intensity factors of a reinforced polymeric composite at different fracture modes. *Int J Eng Sci Appl 5* 7-14 (2021).

[21] Hsieh, T.H., Kinloch, A.J., Taylor, A.C., Kinloch, I.A. The effect of carbon nanotubes on the fracture toughness and fatigue performance of a thermosetting epoxy polymer. *J Mater Sci 46* 7525-7535 (2011) **DOI:10.1007/s10853-011-5724-0**.

[22] Mourad, H.E., Megahed, H., Elshalakany, A.B., Shazly, M. Fracture toughness of glass fiber reinforced polymers with carbon nanotubes fillers at sub-zero temperature. *J Mech Sci Technol 39* 155-163 (2025) **DOI:10.1007/s12206-024-1215-5**.

[23] Parhizgar, S., Zachary, L.W., Sun, C.T. Application of the principles of linear fracture mechanics to the composite materials. *Int J Fract 20* 3-15 (1982) **DOI:10.1007/bf00942161**.

[24] Hosseini, M., Gaff, M., Li, H., Konvalinka, P., Lair, J., Hui, D. et al. A review of the performance of fibre-reinforced composite laminates with carbon nanotubes. *Nanotechnol Rev 12* 20230164 (2023) **DOI:10.1515/ntrev-2023-0164**.

[25] Abot, J.L., Song, Y., Schulz, M.J., Shanov, V.N. Novel carbon nanotube array-reinforced laminated composite materials with higher interlaminar elastic properties. *Compos Sci Technol 68* 2755-2760 (2008) **DOI:10.1016/j.compscitech.2008.05.023**.

[26] Cho, J.R. Comparison of mechanical behaviors between cracked functionally graded GPL- and CNT- reinforced composite plates. *Struct Eng Mech 92* 533-546 (2024) **DOI:10.12989/sem.2024.92.6.533**.

[27] Yildirim, B., Yilmaz, S., Kadioglu, S. Delamination of compressively stressed orthotropic functionally graded material coatings under thermal loading. *J Appl Mech 75* 051106 (2008) **DOI:10.1115/1.2936239**.

[28] Kim, J.-H., Paulino, G.H. Mixed-mode fracture of orthotropic functionally graded materials using finite elements and the modified crack closure method. *Eng Fract Mech 69* 1557-1586 (2002) **DOI:10.1016/s0013-7944(02)00057-7**.

[29] Kaman, M.O. Effect of fiber orientation on fracture toughness of laminated composite plates [0°/θ°]s. *Eng Fract Mech 78* 2521-2534 (2011) **DOI:10.1016/j.engfracmech.2011.06.005**.

[30] Mohammed, A.A.K., Hassan, G.I., Khdir, Y.K. The dynamic behavior of symmetrical laminated nano-composite containing equal numbers of glass and carbon fibre layers. *Stroj Vestn-J Mech E 69* 224-234 (2023) **DOI:10.5545/sv-jme.2022.403**.

[31] Kiran, M.D., Madhu, M.C., Srinivasamurthy, M., Shetty, R.P., Kumar, N., Kadhum, A.A.H. et al. Prediction of fracture toughness parameters of epoxy- carbon fabric-CNT composites using Taguchi's and machine learning approach. *Hybrid Adv 13* 100650 (2026) **DOI:10.1016/j.hybadv.2026.100650**.

[32] Yu, N., Zhang, Z.H., He, S.Y. Fracture toughness and fatigue life of MWCNT/epoxy composites. *Mater Sci Eng A 494*, 380-384 (2008) **DOI:10.1016/j.msea.2008.04.051**.

[33] Cho, J.-R. Numerical evaluation of stress intensity factors in functionally graded CNTRC plates. *KSCE J Civ Eng 26* 4563-4572 (2022) **DOI:10.1007/s12205-022-1237-4**.

[34] Dwivedi, K., Arora, G., Pathak, H. Fatigue crack growth in CNT-reinforced polymer composite. *J Micromech Mol Phys 7* 173-184 (2022) **DOI:10.1142/S2424913022410003X**.

[35] Reddy, J.N. *Mechanics of Laminated Composite Plates and Shells: Theory and Analysis*. 2nd ed., CRC Press (2004) Boca Raton, **DOI:10.1201/b12409**.

[36] Kanagaraj, S., Varanda, F.R., Zhil'tsova, T.V., Oliveira, M.S.A., Simoes, J.A.O. Mechanical properties of high density polyethylene/carbon nanotube composites. *Compos Sci Technol 67* 3071-3077 (2007) **DOI:10.1016/j.compscitech.2007.04.024**.

[37] Bokobza, L. Multiwall carbon nanotube elastomeric composites: A review. *Polymer 48* 4907-4920 (2007) **DOI:10.1016/j.polymer.2007.06.046**.

[38] Ma, X., Scarpa, F., Peng, H.-X., Allegri, G., Yuan, J., Ciobanu, R. Design of a hybrid carbon fibre/carbon nanotube composite for enhanced lightning strike resistance. *Aerosp Sci Technol 47* 367-377 (2015) **DOI:10.1016/j.ast.2015.10.002**.

[39] Hassanzadeh-Aghdam, M.K., Jamali, J. A new form of a Halpin-Tsai micromechanical model for characterizing the mechanical properties of carbon nanotube-reinforced polymer nanocomposites. *Bull Mater Sci 42* 117 (2019) **DOI:10.1007/s12034-019-1784-6**.

[40] Cox, H.L. The elasticity and strength of paper and other fibrous materials. *Br J Appl Phys 3* 72-79 (1952) **DOI:10.1088/0508-3443/3/3/302**.

[41] ANSYS Inc. ANSYS Mechanical APDL Theory Reference Release 2020 R2, Canonsburg, (2020).

[42] Omidi, M., D.T., H.R., Milani, A.S., Seethaler, R.J., Arasteh, R. Prediction of the mechanical characteristics of multi-walled carbon nanotube/epoxy composites using a new form of the rule of mixtures. *Carbon 48* 3218-3228 (2010) **DOI:10.1016/j.carbon.2010.05.007**.

[43] Rafiee, M., Rafiee, J., Wang, Z., Song, H., Yu, Z.-Z. Koratkar, N. Enhanced mechanical properties of nanocomposites at low graphene content. *ACS Nano 3* 3884-3890 (2009) **DOI:10.1021/nn9010472**.

[44] Song, Y.S., Youn, J.R. Influence of dispersion states of carbon nanotubes on physical properties of epoxy nanocomposites. *Carbon 43* 1378-1385 (2005) **DOI:10.1016/j.carbon.2005.01.007**.

[45] Irwin, G.R. Analysis of stresses and strains near the end of a crack traversing a plate. *J Appl Mech 24* 361-364 (1957) **DOI:10.1115/1.4011547**.

[46] Tada, H., Paris, P.C., Irwin, G.R. The stress analysis of cracks handbook, 3rd ed. ASME Press (2000) New York, **DOI:10.1115/1.801535**.

[47] Benthem, J.P., Koiter, W.T. Asymptotic approximations to crack problems. In: Sih, G.C. (ed.), *Methods of Analysis and Solutions of Crack Problems. Mechanics of fracture*, 1. Springer, Dordrecht 131-178 (1973) **DOI:10.1007/978-94-017-2260-5_3**.

[48] Jansen, M., Zuidema, J., Wanhill, R.J.H. *Fracture Mechanics and Engineering Primer*. 2nd ed. (2024) TU Delft Open Publishing, Delft.

**Received** *2026-03-12*, **revised** *2026-08-20, 2026-09-13*,
**accepted** *2026-09-29 as Original Scientific Paper.*

**Data Availability** *The data that support the findings of this study are available from the corresponding author upon reasonable request.*

**Author Contribution** *M.N. Balci: Conceptualization, Methodology, and Writing-Review & Editing; A. Çalışkan: Investigation, Methodology, and Writing-Original Draft; B. Yıldırım: Methodology and Writing-Review & Editing.*

## Analiza loma laminiranih kompozitnih plošč, ojačanih z ogljikovimi nanocevkami (CNT)

**Povzetek** *V raziskavi je obravnavan vpliv ojačitve z ogljikovimi nanocevkami na lomno obnašanje laminiranih kompozitnih plošč. Z uporabo klasične teorije laminiranih plošč in metode korelacije pomikov v kombinaciji z metodo končnih elementov so bili izračunani faktorji intenzivnosti napetosti pri različnih volumskih deležih ogljikovih nanocevk, usmeritvah vlaken, dolžinah razpok in načinih porazdelitve nanocevk. Raziskava obravnava tudi vpliv dejavnikov, povezanih z ogljikovimi nanocevkami, kot sta njihova valovitost in aglomeracija, na faktor intenzivnosti napetosti v različnih kompozitnih strukturah. Za določitev ustrezne velikosti končnih elementov je bila izvedena analiza konvergence mreže. Rezultati so bili primerjani s podatki iz literature, pri čemer je bilo ugotovljeno zelo dobro ujemanje. Primerjava potrjuje ustreznost uporabljene metode in dokazuje, da je mogoče z metodo korelacije pomikov natančno izračunati faktorje intenzivnosti napetosti ter raziskovati lomno obnašanje kompozitov, ojačanih z nanocevkami. Vpliv dodajanja ogljikovih nanocevk na lomno obnašanje laminiranih kompozitov, ojačanih z ogljikovimi vlakni, doslej še ni bil obravnavan s predlaganim računskim pristopom, kar predstavlja novost raziskave. Parametrične analize kažejo, da ojačitev z ogljikovimi nanocevkami pomembno vpliva na faktor intenzivnosti napetosti. Ta vpliv se spreminja glede na kot usmeritve vlaken, ki ima, kot kaže, večji vpliv na faktor intenzivnosti napetosti kot delež nanocevk. Glavne ugotovitve kažejo, da lahko dodajanje ogljikovih nanocevk do določenega deleža zmanjša faktor intenzivnosti napetosti v kompozitih, zlasti kadar obremenitev deluje v smeri vlaken. Rezultati lahko prispevajo k ustrezni izbiri deleža ogljikovih nanocevk za izboljšanje lomnega obnašanja teh struktur.*

**Ključne besede** *ogljikove nanocevke (CNT), klasična teorija laminiranih plošč, metoda korelacije pomikov (DCT), efektivni kompozitni laminat, faktor intenzivnosti napetosti (SIF)*